

Influence of average size and interface passivation on the spectral emission of Si nanocrystals embedded in SiO₂

B. Garrido Fernandez,^{a)} M. López, C. García, A. Pérez-Rodríguez, and J. R. Morante
Department d'Electrònica, EME, Universitat de Barcelona, Martí i Franquès 1, 08028 Barcelona, Spain

C. Bonafos, M. Carrada, and A. Claverie
CEMES-CNRS, 29 rue J. Marvig, 31055 Toulouse, France

(Received 25 July 2001; accepted for publication 8 October 2001)

The correlation between the structural (average size and density) and optoelectronic properties [band gap and photoluminescence (PL)] of Si nanocrystals embedded in SiO₂ is among the essential factors in understanding their emission mechanism. This correlation has been difficult to establish in the past due to the lack of reliable methods for measuring the size distribution of nanocrystals from electron microscopy, mainly because of the insufficient contrast between Si and SiO₂. With this aim, we have recently developed a successful method for imaging Si nanocrystals in SiO₂ matrices. This is done by using high-resolution electron microscopy in conjunction with conventional electron microscopy in dark field conditions. Then, by varying the time of annealing in a large time scale we have been able to track the nucleation, pure growth, and ripening stages of the nanocrystal population. The nucleation and pure growth stages are almost completed after a few minutes of annealing time at 1100 °C in N₂ and afterward the ensemble undergoes an asymptotic ripening process. In contrast, the PL intensity steadily increases and reaches saturation after 3–4 h of annealing at 1100 °C. Forming gas postannealing considerably enhances the PL intensity but only for samples annealed previously in less time than that needed for PL saturation. The effects of forming gas are reversible and do not modify the spectral shape of the PL emission. The PL intensity shows at all times an inverse correlation with the amount of P_b paramagnetic centers at the Si–SiO₂ nanocrystal–matrix interfaces, which have been measured by electron spin resonance. Consequently, the P_b centers or other centers associated with them are interfacial nonradiative channels for recombination and the emission yield largely depends on the interface passivation. We have correlated as well the average size of the nanocrystals with their optical band gap and PL emission energy. The band gap and emission energy shift to the blue as the nanocrystal size shrinks, in agreement with models based on quantum confinement. As a main result, we have found that the Stokes shift is independent of the average size of nanocrystals and has a constant value of 0.26 ± 0.03 eV, which is almost twice the energy of the Si–O vibration. This finding suggests that among the possible channels for radiative recombination, the dominant one for Si nanocrystals embedded in SiO₂ is a fundamental transition spatially located at the Si–SiO₂ interface with the assistance of a local Si–O vibration. © 2002 American Institute of Physics.

[DOI: 10.1063/1.1423768]

I. INTRODUCTION

Many researchers have tried to elucidate the origin of the visible–near infrared photoluminescence (PL) emission at room temperature of silicon nanostructures. This is due to their promising perspective as silicon-compatible optoelectronic materials. In particular, structures consisting of Si nanocrystals embedded in SiO₂ are candidates for a large number of optoelectronic and photonic applications.¹ The advantages of the Si–SiO₂ composites rely on their robustness and surface stability in comparison with porous materials and on their full process compatibility with mainstream complementary metal–oxide–semiconductor (CMOS) technology. Si nanocrystals embedded in SiO₂ have been fabricated by a variety of methods and include techniques such as

cosputtering,² ion implantation,³ chemical vapor deposition,⁴ molecular beam epitaxy,⁵ and laser ablation.⁶ Among these techniques, ion implantation is one of the most suitable choices due to its ability to control the profile of the implanted ions.

The opening of the band gap when the nanocrystal size shrinks is nowadays an unquestionable fact for both porous Si layers and Si nanocrystals embedded in SiO₂.^{7–10} This opening arises as a consequence of the quantum confinement of carriers in the three dimensional potential well of the nanocrystal. The photon absorption process in a typical PL experiment proceeds in the core of the nanocrystal and, as a fundamental transition from valence to conduction band, its energy is modulated by quantum confinement effects. The PL emission reported for Si–SiO₂ systems consists of an intense (visible with the naked eye) and wide (about 0.3 eV) emission peaking in the near infrared or the visible spectrum (be-

^{a)} Author to whom correspondence should be addressed; electronic mail: blas@el.ub.es

tween 1.4 and 1.9 eV). This emission has been unambiguously linked to the presence of Si nanocrystals in an oxide matrix.^{3,8,11–26} Nevertheless, the mechanism of the dominant radiative recombination mechanism is still under debate, as in porous silicon.

It is obvious that the correlation between the structural (average nanocrystal size, density, and volume fraction) and the optoelectronic properties (band gap and PL emission) of the Si–SiO₂ composites is an essential factor to understand their emission mechanism. This correlation has been very difficult to establish in the past due to the lack of reliable methods for measuring the size distribution of nanocrystals from electron microscopy, mainly because of the insufficient contrast between Si and SiO₂. Some authors have used scanning probe microscopes for measuring the size of deposited nanocrystals²⁵ and others used indirect techniques such as Raman spectroscopy.²⁶ Recent studies by other authors and us have overcome this difficulty and shed light on the explanation and identification of the dominant mechanism of radiative recombination. In particular, we have recently developed a successful method for imaging Si nanocrystals in SiO₂ matrices. This has been done by using high-resolution electron microscopy (HREM) in conjunction with conventional electron microscopy in dark field conditions and will be explained below.^{27–30}

The dominant mechanisms for the PL emission of H-passivated porous Si are considered to be direct band to band radiative recombination, due to the breakdown of the \mathbf{k} conservation rule, and/or indirect recombination assisted by Si phonons.^{9,10,25} Resonantly excited PL in H-terminated porous silicon clearly shows steps that coincide with the TO and TA phonons of silicon. In contrast, Si nanocrystals embedded in SiO₂ show an emission more intense and shifted to the red in comparison with porous silicon nanostructures of roughly the same size. Resonantly excited PL of oxidized nanocrystals does not present steps due to Si phonons, as reported by Kanemitsu and Okamoto¹³ On the contrary, they show small steps that agree roughly with the energy of SiO₂ vibrational modes. Allan *et al.*³¹ speculated on the existence of intrinsic localized states at the Si–SiO₂ interface in the form of self-trapped excitons. So, there seems to be a consensus nowadays for nanocrystals embedded in SiO₂ in that the interface does have an active and dominant role in their emission mechanism. This is possible either through the existence of interfacial radiative states²⁶ or because of vibronic interactions among electron–hole pairs created in the nanocrystals, and the polarizable material surrounding them. We have recently proposed the assistance of Si–O vibrations at the interface as the possible dominant path for the recombination of electron–hole pairs in Si nanocrystals embedded in SiO₂.¹⁶ The interfaces are so important that its passivation against nonradiative states and defects is necessary to increase the radiative yield of the emission of Si nanocrystals, with independence of the emission mechanism. There are some reports on the increase of radiative efficiency by performing H passivation through standard forming gas annealing.^{32–34} This way of passivating the Si–SiO₂ interface is well known and is routinely performed in CMOS technology. However, there is still no report on the quantifi-

cation of the passivation effect and the correlation among defect concentration and PL yield.

The purpose of this article is to contribute to the explanation of the PL emission mechanism of ion beam synthesized Si nanocrystals embedded in SiO₂. We report on a systematic study of the evolution of PL emission and absorption features of nanocrystals versus implantation dose and annealing conditions and the measurement of reliable size distributions from electron microscopy. Based on these studies, we find a correlation between the structural and optical properties of Si nanocrystals. From the experimental data, we calculate the Stokes shift as a function of the average size and propose a likely explanation for the dominant emission mechanism in this system. We also show from electron spin resonance (ESR) experiments that the PL intensity inversely correlates with the amount of P_b centers at the Si–SiO₂ interfaces. In fact, for the annealing temperatures used in this work (1100 °C), the nucleation and pure growth of the nanocrystals proceed almost instantly. The interface rearranging and the passivation of P_b centers control the PL yield for the rest of the annealing time. This is confirmed by additional annealing in forming gas, which increases the PL yield and diminishes the P_b signal at the same time. Furthermore, the effects of forming gas treatments are reversible and do not modify the spectral shape of the PL emission.

II. EXPERIMENTAL DETAILS

Silicon nanocrystals were synthesized by ion implantation of Si⁺ in relatively thick SiO₂ layers (800 nm) grown by wet oxidation at 1100 °C on *p*-type Si (100). The samples were implanted with doses ranging from 1×10^{16} to 3×10^{17} Si⁺ ions/cm². The implantation energy was 150 keV and the samples were kept at room temperature during the whole process. The projected range of the ion implantation and the initial supersaturation were calculated by using the TRIM code. The projected range was of about 200 nm and the silicon excess (supersaturation) ranged from 1 to 30 at. % at the maximum of the implantation profile. The as-implanted samples were submitted to thermal treatments at 1100 °C in N₂ for durations from 1 min to 16 h (in rapid thermal and conventional furnaces). With such a wide range of annealing time, we probed the evolution of the precipitates all through the nucleation, pure growth, and ripening stages. Thick SiO₂ layers were preferred to avoid interface effects on the nucleation and growth of the nanocrystals. This is accomplished if interfaces are several diffusion lengths away from regions with significant silicon supersaturation. This has always been the case in our experiments, even for the longest annealing times (Si diffusion coefficient in SiO₂ at 1100 °C is about 10^{-17} cm²/s).

HREM was used to monitor the size distribution of nanocrystals and its evolution with dose and annealing time. Unfortunately, the poor contrast between Si and SiO₂ made those measurements extremely difficult and very time consuming except for the high supersaturation values (10%–30%). Nevertheless, previous studies made by us with Ge nanocrystals in SiO₂ (better contrast) and atomistic simulations recently developed by us shed light on many issues

related to the nucleation and growth of group IV nanocrystals in SiO_2 . These studies can be used to infer and extrapolate tendencies whenever HREM analysis is not suitable for the Si– SiO_2 system (low silicon supersaturation).^{27–30} ESR experiments were performed at room temperature using conventional absorption ESR at 9.1 GHz and employing a 100 kHz field modulation when detecting the first derivative of absorption. The spin density of paramagnetic centers was obtained by numerical integration of the first derivative absorption and a comparison with a reference signal. The samples were cut into pieces and the absolute surface density of paramagnetic centers was determined by weighing the samples in a microbalance. The ESR measurements allowed us to successfully determine and quantify the evolution of the amount of paramagnetic defects in the SiO_2 and at the Si– SiO_2 interface as a function of annealing time and to correlate this evolution with the photoluminescence intensity.

We have performed systematic PL and PL excitation (PLE) measurements in all samples. Several experimental setups were combined. For optical pumping in PL measurements we have used a 60 mW He–Cd laser for ultraviolet excitation ($\lambda=325$ nm). The luminescent emission was analyzed in backscattering mode by a 0.6 m monochromator and detected with a GaAs photomultiplier. The standard chopper–lock in technique was used to increase the signal to noise ratio. All the measurements were corrected for the system response measured with a calibrated tungsten lamp. The energy provided by the He–Cd laser (3.82 eV) is able to excite the whole nanocrystal distribution down to diameters of about 1 nm. For PLE measurements, we used a 1 kW ultraviolet Xe lamp with a broad and flat emission spectrum. In general, PLE measurements provide a relative measure of absorption, and the signal is proportional to the absorption coefficient in the optically thin regime ($\alpha d \ll 1$) which applies to all our measurements.

III. THE GROWTH OF SI NANOCRYSTALS IN SiO_2 MATRICES

A. Experimental evidence of phase separation

Fourier transform infrared spectroscopy (FTIR) and x-ray photoelectron spectroscopy (XPS) combined measurements show that most of the silicon in excess has precipitated after 1 min of annealing time at 1100 °C in N_2 . Both techniques are complementary since FTIR probes the oxide matrix while XPS detects Si and SiO_x suboxides. FTIR absorption spectra show that the asymmetric stretching mode of the Si–O–Si unit (TO_3 mode) shifts to lower frequencies in the as-implanted samples. This is because the Si^+ ion implantation outcome is a damaged and substoichiometric oxide matrix. Nevertheless, the TO_3 mode regains the same position of nonimplanted control oxides (thermal SiO_2) after only 1 min of annealing time (see Fig. 1). The XPS spectra of the Si $2p$ band (not shown) present two well resolved peaks situated at 99.4 eV (Si in Si, i.e., Si– Si_4) and 103.4 eV (Si in SiO_2 , i.e., Si– O_4). This is characteristic of a Si– SiO_2 composite with separated phases. However, a relatively small XPS signal coming from suboxides is observed in the spectra. It is likely that this signal comes from the interface be-

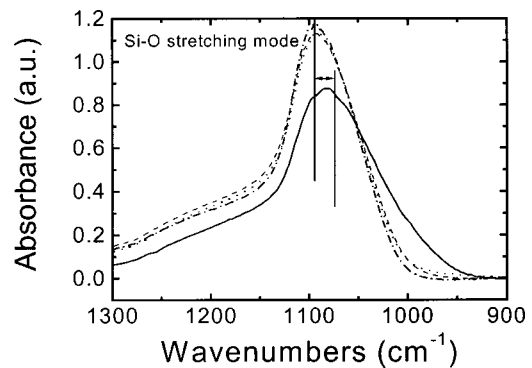


FIG. 1. FTIR spectra of samples implanted with 10% supersaturation and annealed at 1100 °C during 1 min (dashed line) and 8 h (dotted line), and as-implanted sample (solid line). For reference, the FTIR spectrum of a nonimplanted oxide is also shown (dash-dotted line).

tween the crystallites and the matrix (for detailed descriptions of XPS and FTIR spectra of implanted oxides see Ref. 35).

B. Electron microscopy imaging conditions

The imaging of Si nanocrystals embedded in SiO_2 by conventional TEM is difficult because of the small difference of atomic number and density between Si and SiO_2 . Therefore, Si nanocrystals in SiO_2 show only weak amplitude and phase contrast. HREM (high resolution) is routinely used to image individual Si nanocrystals. However, it is not necessarily the best imaging technique when quantitative and statistical measurements have to be performed. A HREM image of a Si nanocrystal is shown in the inset of Fig. 2. Building up size histograms from HREM images is a difficult task and reproducible results are difficult to obtain. In fact, the probability of imaging a nanocrystal depends on different factors. On the one hand, for very thin regions, the probability of forming fringes when imaging along a random direction increases as the size of the particle decreases (the so-called “potential opening up effect”).³⁶ On the other hand, the contrast arising from small particles is more easily lost in the noise when the thickness of the overall sample increases.

Recently, Iacona *et al.*³⁷ and the present authors³⁰ used conventional dark field (DF) to image high densities of Si nanocrystals. The contrast arising from such images is due to

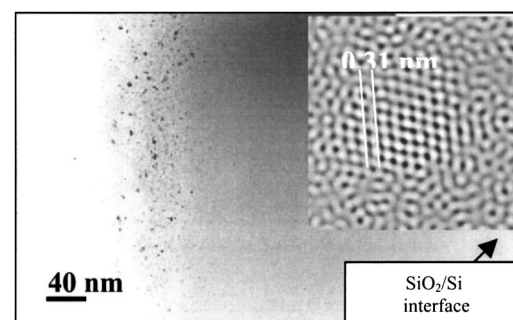


FIG. 2. DF conventional image of the sample with 30% supersaturation annealed at 1100 °C for 4 h, where the spatial distribution of the nanocrystals with good contrast can be appreciated. (Inset) the high resolution image of an individual Si nanocrystal.

the diffraction of the electrons by the atomic planes of those nanocrystals having their (111) planes well oriented with respect to both the incident beam and the aperture. Such an image is shown in Fig. 2. The main advantage of DF imaging conditions is to observe the Si nanocrystals at a lower magnification. This allows imaging the spatial distribution of the nanocrystals within the SiO₂ layer. Moreover, under these conditions, the probability of “seeing” a nanocrystal does not depend much on its size.

In our HREM images, the resolution is of about 0.2 nm. So, in principle, two diffracting planes at a distance greater than this can be separated and imaged. Nevertheless, experience shows that nanocrystals with a diameter of less than four planes (about 1.2 nm) are very difficult to distinguish from the SiO₂ matrix.^{29,30} In DF images, the resolution is in principle of about a 1 nm higher value than for HREM, but Si nanocrystals exhibit stronger contrast. Furthermore, the observations under DF conditions are less dependent of the thickness of the observed region, much less time consuming, and finally, good statistical results can be easily obtained with high reproducibility. The error bars for the size measurement have been evaluated to be of about 20% for both for HREM and DF imaging conditions. All the size measurements have been systematically performed in both DF and HREM images and the final diameter is a mean value of both measurements.

C. Electron microscopy results: Average sizes

We have seen above that Si nanocrystals can only be imaged in orientation dependent conditions (HREM or DF). Thus, we were not able to see all the precipitates in the same image and we could not evaluate which fraction of the whole population they represented. Consequently, the density of precipitates could not be measured for this system. However, we were able to measure the density of Ge nanocrystals in SiO₂ (stronger contrast than Si) that can be imaged under bright field conditions, which are orientation independent. For this system, an original method for density measurements was developed and tested.^{27,28} As a result, we showed that Ge nanocrystals undergo a conservative Ostwald ripening during annealing.

Figure 3 shows the Si nanocrystal mean diameter as a function of annealing time at 1100 °C. The results are shown only for the higher 10%, 20%, and 30% values of supersaturation because of the visibility reasons given above. The mean diameter increases very slowly, almost imperceptibly, when the annealing time changes from 1 min to 16 h. This very slow evolution is consistent with an asymptotic conservative Ostwald ripening evolution of the nanocrystals, as reported for Ge nanocrystals previously.^{27,28} This is also consistent with the very small values reported for the diffusion coefficient of Si in SiO₂: from 5×10^{-18} to 10^{-16} cm²/s at 1100 °C depending of the authors.^{38,39} On the contrary, for a fixed annealing time such as 16 h, the mean diameter increases roughly from 3 to 5 nm when the supersaturation changes from 10% to 30%. This remarkable increase of diameter versus supersaturation is in strong contrast with the standard Ostwald ripening theory, which predicts a final di-

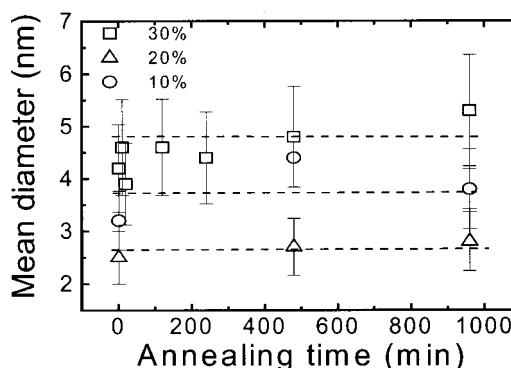


FIG. 3. Evolution of the average diameter of the nanocrystal population extracted from TEM measurements, as a function of the annealing time at $T = 1100$ °C, for initial Si supersaturation of 10%, 20%, and 30%. The values of the error bars are approximately 20% of the absolute values. Dashed lines are only a guide for the eye.

ameter that is independent of the initial supersaturation. However, the Ostwald ripening theory has been developed for much more diluted systems. For the 20% and 30% supersaturation the average distance between the surfaces of nanocrystals is so small (less than 1 nm), that one should consider proximity effects for a reasonable ripening model.

D. Modeling the ripening of Si nanocrystals in SiO₂

In order to explain the experimental results, we have modeled the ripening of Si nanocrystals by using an “atomistic” model. This model is inspired by the one developed by Cowern *et al.*⁴⁰ for linear extended defects in Si, but applied here to spherical objects. In a first approach, we have made the following assumptions: (i) We consider the so-called “mean-field” approximation to be valid, i.e., there is no interaction between nanocrystals (diluted system). (ii) The initial supersaturation has already formed particles of size 2 (atoms, i.e., a Si–Si cluster) at the beginning of annealing. Indeed, for the large supersaturation values considered here, the formation of small Si clusters is very probable even in the as-implanted state.⁴¹ (iii) We apply the quasisteady state approximation in which the precipitates and the matrix are in local equilibrium since the beginning of annealing. (iv) The effect of the air–SiO₂ surface of the sample as a sink has been tested and can be considered as negligible because of the low diffusivity of Si in SiO₂ and the high density of nanocrystals. We will not go into details and equations here, but the interested reader can consult Refs. 30 and 41.

In Fig. 4(a) we have represented the results obtained from this first approximation of the atomistic model by a solid curve. This curve depicts the simulated mean diameter, which is independent of the initial supersaturation (diluted system). We have superimposed the TEM experimental values with symbols, as in Fig. 3. As expected, the simulated mean diameter increases steadily with annealing time. This theoretical mean diameter fits the TEM values only for 10% of the supersaturation and for long annealing times (several hours). As shown in Fig. 5(a), the size distribution obtained from the simulations (solid curve) is in good agreement with the TEM stack histogram, even better than the well-known Lifshitz, Slyosov, and Wagner analytical distribution.⁴² The

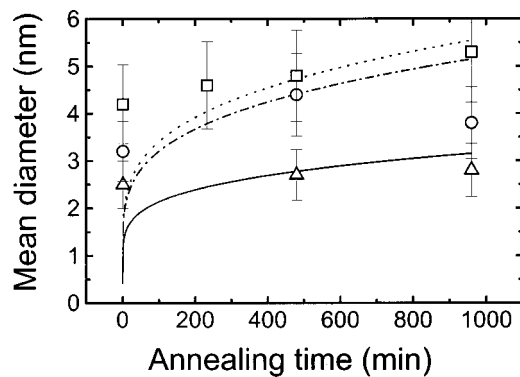


FIG. 4. Experimental values (symbols) and simulated values (curves) of the mean diameter of the nanocrystal population for the samples with 10% (triangles), 20% (circles), and 30% (squares) of supersaturation. It is clearly seen that the curves of the model that take into account proximity effects fit all the supersaturation values rather well, at least for long annealing times.

experimental values of size found for the 20% and 30% supersaturation are much higher than those predicted by the simulation. We can thus infer that, as suspected for high supersaturation, the growth rate is augmented by proximity effects and the diluted system approximation is no longer valid. The good correlation of the theoretical and experimental size distributions is a strong indication that the amount of nanocrystals with diameter smaller than the resolution of the microscope (and then not seen) is small.

In Ref. 30 we have developed a correction of the “atomistic” simulation valid for interacting nanocrystals, which the reader should consult for details. For large initial supersaturation, the distance between nanocrystals is no longer negligible compared to the dimension of the particles. Then, we take into account the overlapping gradients of supersaturation at the precipitate neighborhood. The essential point is to survey the size of the region that is likely to act as a source or sink for the excess of solute atoms. We have imaged this

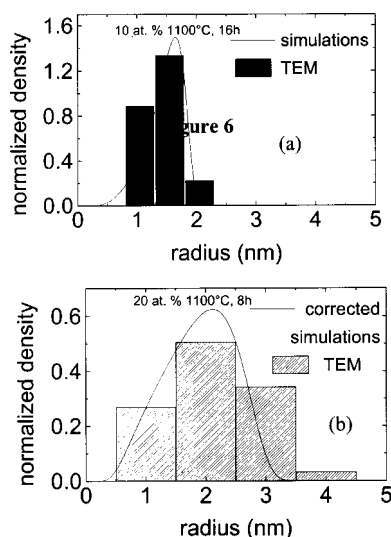


FIG. 5. Simulated size distributions superimposed on the transmission electron microscopy (TEM) stack histograms. (a) The sample of 10% supersaturation annealed at 1100 °C for 8 h. (b) The sample of 20% supersaturation annealed at 1100 °C for 16 h (here the corrected model for nanocrystal interaction is used).

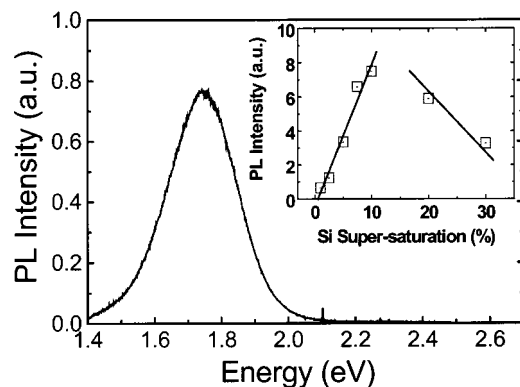


FIG. 6. Typical spectrum of PL emission. In this particular case, the sample is that of the 10% supersaturation and annealed for 8 h. (Inset) The integrated PL vs supersaturation in the whole range from 1% to 30%.

region as a sphere of influence having a radius, which is related to the mean distance between the precipitates.^{30,43,44} When the density of nanocrystals is high enough, the spheres of influence overlap and, therefore, the supersaturation of the matrix and the emission and capture rates of solute atoms by the nanocrystals are functions of the distance between them.

We have also represented in Fig. 4 the evolution of the simulated mean diameter [dashed curves (b) and (c)] for 20% and 30% of supersaturation, taking into account the interaction between nanocrystals. The simulations now agree well with the TEM results for long annealing times, independently of the initial Si supersaturation. The simulated size distribution for the 20% sample is shown in Fig. 5(b). It is clear in this figure that the significant enlargement of the TEM stack histogram is due to proximity effects. The only disagreement between theory and experiment concerns the short annealing times, where the measured sizes are much larger than the predicted ones. This experimental finding is in agreement with the FTIR and XPS measurements presented above in Sec. III A), as it means that almost all the Si in excess has precipitated at the beginning of annealing. So far, the resolution of the TEM is probably not the limiting factor, because of the good agreement with the simulated histograms. One possible reason is having assumed in the simulation the equilibrium between the precipitates and the surrounding supersaturation already at the beginning of annealing. It is probable that this local equilibrium is preceded by a rapid transient “pure growth regime” taking place during the first minute of annealing time.

IV. PHOTOLUMINESCENCE VERSUS STRUCTURE FOR Si NANOCRYSTALS IN SiO₂

A. Photoluminescence versus supersaturation and link with structure

All the annealed samples are characterized by a strong and wide (about 0.3 eV at half maximum) PL emission extended through the red and near infrared. The PL emission is always visible with the naked eye under ordinary laboratory illumination and is comparable with the PL intensity of porous Si. The typical spectral dependence of PL emission is shown in Fig. 6. In the inset of this figure, we have repre-

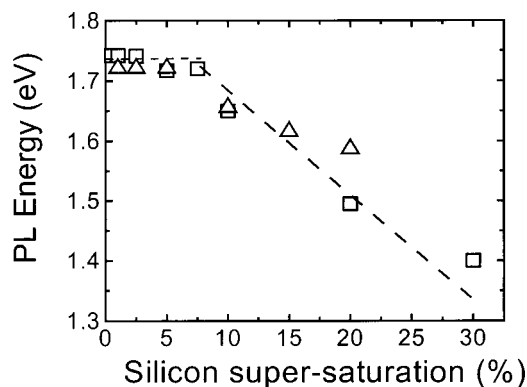


FIG. 7. Evolution of the PL peak energy position as a function of the atomic supersaturation: (squares) this work, (circles) measurements done by Iwayama *et al.* (See Ref. 8).

sented the evolution of PL intensity with Si supersaturation for samples annealed 8 h at 1100 °C in N₂, that is to say, well into the ripening stage. The linear dependence of PL intensity versus supersaturation in the range from 1% to 10% is highly remarkable. Taking into account the modeling performed in Sec. III D, we shall call this range “dilute supersaturation” because there is no interaction between nanocrystals during the ripening stage. Nevertheless, for the high supersaturation of 20% and 30%, in the “nondiluted range” where the nanocrystals interact during ripening there is a substantial decrease of PL intensity.

Figure 7 shows the peak position of PL emission as a function of supersaturation, where the data of this work are the squares and the data from other authors are the triangles.⁸ It is clearly shown that the peak position is of about 1.7 eV for dilute supersaturation while it steadily shifts to the infrared with increasing supersaturation down to 1.4 eV for the 30% supersaturation. Thus, this is another hint that there is a clear delineation in both structural and optical emission properties when the system evolves from being a dilute one with no interaction among nanocrystals to becoming a non-dilute interacting one.

The link of PL with structural characterization by electron microscopy (TEM) can be made at this stage. For the dilute range from 1% to 10% of supersaturation, the Ostwald ripening theory predicts and our atomistic simulation confirms that the average size of nanocrystals is independent of supersaturation. The average nanocrystal diameter measured by TEM is of about 3.0 nm for the 10% and following the theory, it would be the same for all the samples in the diluted range. Thus, the linear increase of PL intensity with supersaturation can be understood as a linear increase of PL intensity with the density of available nanocrystals. The fact that the mean size would remain constant in the diluted supersaturation range also explains the constant value found for the PL emission energy. On the contrary, interaction between nanocrystals must be taken into account to explain the average diameter dependence on supersaturation for the 20% (3.8 nm) and 30% (5.3 nm). The atomistic simulation modeling taking into account proximity effects predicts this behavior, as shown above. This increase of the mean diameter explains the remarkable shift of the PL peak emission to the infrared

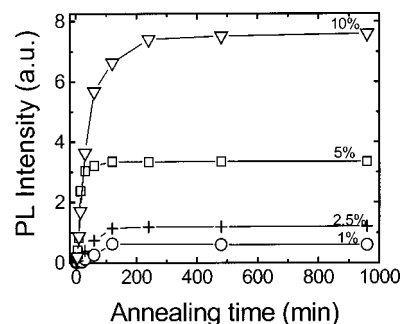


FIG. 8. PL intensity as a function of annealing time, with initial supersaturation between 1% and 10% as a parameter. The samples of the 20% and 30% supersaturation show exactly the same behavior, but the intensity drops to values comparable to 5% and 1%, respectively.

for these samples: to 1.5 eV for the 20% and to 1.4 eV for the 30%. This result is compatible with quantum confinement effects in the PL emission. It also can explain the decrease of PL intensity for Si supersaturation higher than 10%. The reason is probably because large nanocrystals have smaller cross section (per Si unit cell) for absorption and the theory also predicts a smaller transition rate (oscillator strength) for such large sizes, although no experimental proof still exists for this interpretation.^{45,46}

B. Photoluminescence intensity versus annealing time and link with structure

The time evolution of PL intensity during annealing presents two distinct regimes, which are shown in Fig. 8. (i) An initial fast increase (transient stage) that bends over after 3–4 h of annealing time at 1100 °C and (ii) a completely flat dependence (saturation stage) for longer annealing times up to 16 h. The PL intensity saturation is explained satisfactorily by the asymptotic Ostwald ripening stage of the nanocrystal population. As the diffusion coefficient of Si in SiO₂ is very small, the ripening stage is so slow that the population of nanocrystals is nearly “frozen.” Nevertheless, the time region where the PL intensity increases (transient) cannot be understood only as a consequence of the nucleation and/or pure growth of the nanocrystals. In fact, even after 1 min of annealing time, we have seen that these stages are over and the average diameter remains almost constant for the rest of the annealing time. Consequently, one must invoke a kind of rearranging of interface and/or passivation of nonradiative defects to explain the transient stage. We shall demonstrate quantitatively this connection in the next section.

C. Interface passivation and its influence in photoluminescence emission yield

If the pure growth stage is over after 1 min of annealing time at 1100 °C, a rearranging and passivation of nonradiative defects at the interface must take place to account for the further increase of PL intensity. We have performed ESR experiments to evaluate the role of passivation in the PL intensity curve versus annealing time. The as-implanted samples exhibit a broad ESR feature with a gyromagnetic factor (g) centered at 2.001 (see Fig. 9). This is the characteristic signature of the E' centers and their variants.⁴⁷ These

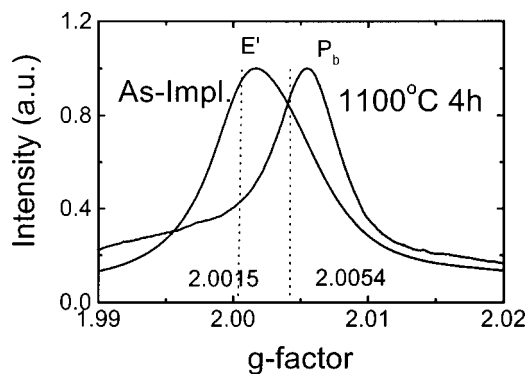


FIG. 9. ESR absorption spectra of the sample implanted with a supersaturation of 10%. The E' defect ($g=2.00158$) is detected only in the as-implanted sample. The sample annealed at 1100°C for 4 h does not present this kind of defect. A different spectrum appears, centered at 2.0052 and related to P_b centers.

defects are O vacancies relaxed and positively charged in SiO_4 tetrahedra. The E' defects completely disappear in all the annealed samples. These samples show g factor shifts to a value around $g=2.005$ (Fig. 9), which corresponds to the characteristic signature of the well-known P_b centers.⁴⁸ These centers are Si dangling bonds located at the Si– SiO_2 interfaces.

In Fig. 10 we have represented the kinetic evolution with annealing time of both the PL intensity and the integrated signal coming from the P_b centers. These measurements have been previously reported by us.^{15,17} The strong inverse correlation can be interpreted in the following way. During the first minutes of annealing time the nanocrystal ensemble is finishing the growth stage, the remaining Si supersaturation in the matrix is declining quickly, and Si– SiO_2 interfaces begin to form. This is why E' defects in the oxide are wiped out and P_b centers appear as soon as well-delineated Si– SiO_2 interfaces are formed. The signal coming from P_b centers is then expected to rapidly increase with annealing time in this region. For the rest of the annealing duration, the concentration of P_b centers and the PL intensity are clearly inversely correlated and both signals saturate at roughly the same annealing time (about 3–4 h). This additional anneal-

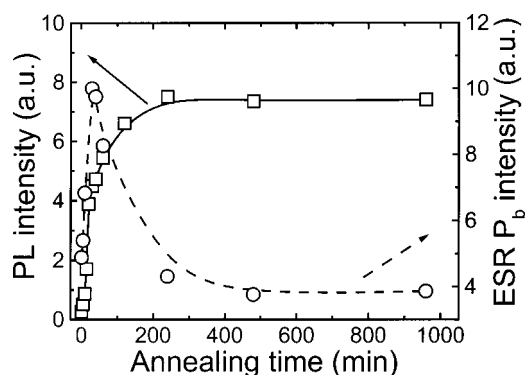


FIG. 10. PL intensity vs annealing time at 1100°C in N_2 for a sample of 10% supersaturation (left axis). Evolution of the amount of P_b interfacial centers for the same sample measured from ESR (right axis).

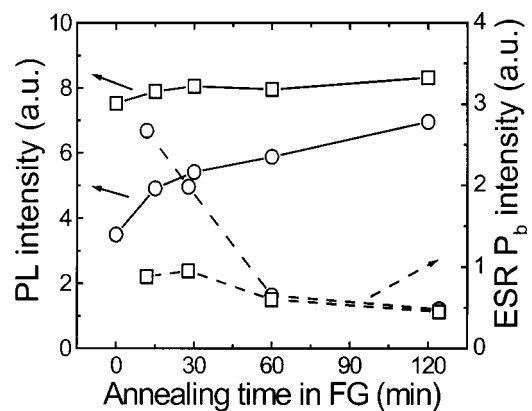


FIG. 11. Correlation between the PL intensity (left axis) and the amount of P_b centers measured from ESR vs forming gas annealing duration for the sample of 10% supersaturation. Squares correspond to the sample annealed previously at 1100°C for 8 h and the circles correspond to the sample annealed previously at 1100°C for 20 min.

ing time at 1100°C improves and passivates the Si– SiO_2 interface in such a way that a great number of defects are annealed out.

An unambiguous correlation between the PL intensity coming from nanocrystals and an ESR signal coming from a specific defect have been reported for Si nanocrystals embedded in SiO_2 . Nevertheless, we should mention here that other studies were previously released on the correlation of ESR data and PL of porous silicon, although the kind of defects and interfaces observed are different from these studied here.^{49–52}

Then, for the nanocrystals embedded in SiO_2 , we can conclude that P_b centers or centers intimately related to them are radiative recombination killers and that suitable treatments to diminish them can dramatically increase the PL yield. As shown in Fig. 10, long annealing treatments at high temperature in N_2 improves the yield up to a saturation value. Indeed, postoxidation annealings at high temperature are frequent in CMOS technology to improve the quality of the Si– SiO_2 interface. Alternatively, hydrogen passivation of defects and dangling bonds through forming gas annealing treatments is a suitable alternative with a lower thermal budget.

We have studied the effects of forming gas postannealing at 450°C on two samples, selected from different regions of the PL kinetic curve (the transient and steady state regions). The PL and ESR curves for both of them are shown in Fig. 11. We observe that the PL increase of the sample in the PL transient region (20 min) is much more important than the PL increase of the sample in the saturation region (8 h), where in fact the PL intensity remains almost constant. The forming gas treatment is capable of enhancing the PL intensity. However, it seems that it only brings PL close to the level of saturation for very long conventional annealing at 1100°C . The concomitant decrease of the ESR signal of P_b centers is additional proof of the inverse correlation between PL intensity and the amount of interfacial P_b centers.

We have found the effects of the forming gas treatments to be reversible. Indeed, samples annealed at temperatures in excess of 500°C release part of the H and the PL yield di-

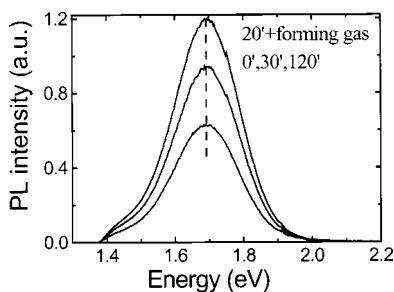


FIG. 12. Sample with 10% supersaturation, annealed 20 min at 1100 °C in N₂ (transient range) and postannealed in forming gas for 0, 30, and 120 min. The intensity increases with forming gas annealing time but the peak position and the spectral dependence are exactly the same for all of them.

minishes. In particular, annealings of passivated samples performed at higher temperature and in vacuum conditions decrease the PL yield. This is in fact a method reported in the literature to create P_b centers for studying them.⁵³ This is an additional presentation of evidence of the correlation among the PL yield and the amount of P_b centers. Furthermore, we have observed (Fig. 12) that the forming gas annealing treatments only increase the intensity of the PL emission. There is no modification at all in the peak energy or the spectral shape of the PL emission.

V. BAND GAP VERSUS SIZE AND SUGGESTION OF A RADIATIVE RECOMBINATION CHANNEL

The PLE measurements were performed using a continuous wavelength excitation source (Xe lamp) and fixing the detection monochromator at the peak position of the previously measured PL spectra. The PLE spectra mimics the absorption coefficient if the layer is thin and if relaxation time from the excitation to the emitting level is negligible in comparison with the time response of PL. This is the situation in our samples as the PL transient response was of about 200 μs from the nearly resonant excitation (about 2 eV) up to the detection limit of the optical system (about 4 eV). The Stokes shift between PL and PLE is clearly noticed in Fig. 13. The PLE signal only begins to be important for energies above 2.2 eV. The PLE spectra are smooth, quadratic with energy, and featureless, like the onset of absorption of an

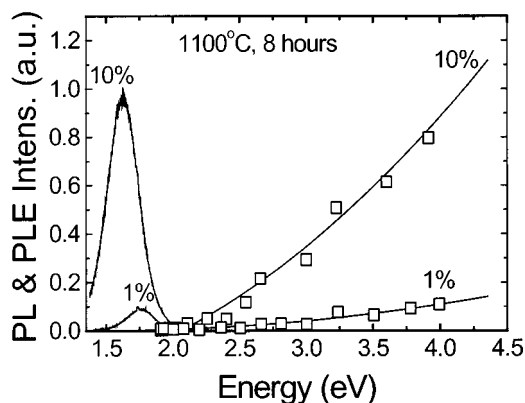


FIG. 13. PL and PLE spectra of samples with silicon supersaturation of 1% and 10%.

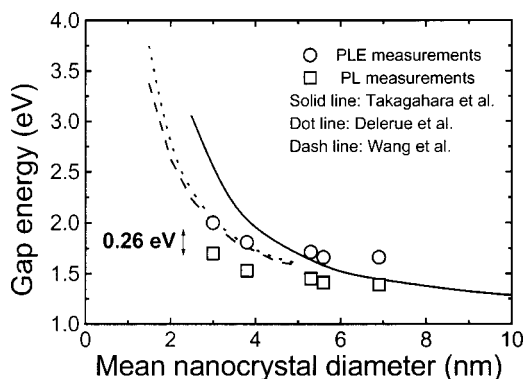


FIG. 14. Theoretical data for the band-gap energy as a function of nanocrystal diameter: the full line is the effective mass approximation of Takagahara and Takeda (see Ref. 56); the dashed-lines are the pseudopotential calculations of Wang and Zunger (see Ref. 55) and the dotted line are the linear combination of atomic orbital calculations by Delerue *et al.* (see Ref. 54). The experimental results of this work are the band gaps (squares) and the photoluminescence peak positions (circles).

indirect band-gap semiconductor as Si. So we must admit that even for these small sizes, silicon still remains basically an indirect band-gap semiconductor. Thus, as usually made for indirect band-gap semiconductors, an average value of the band gap is obtained from the intersection of the Tauc plot of $\sqrt{I_{\text{PLE}} \times E}$ with the E axis.¹⁶

The oscillator strength or radiative recombination probability increases when the diameter of the nanocrystal shrinks. This fact is predicted by theoretical calculations and affects mainly the PL response for quasidirect (zero-phonon) transitions. These transitions are partially allowed in nanocrystals because spatial confinement leads to the spread of \mathbf{k} in the reciprocal space. This means that for direct transitions, smaller nanocrystals will contribute more to the PL emission than large nanocrystals. In such a case, the band gap obtained from the Tauc plot will always overestimate the average band gap of the nanocrystal distribution. These quasidirect fundamental transitions or indirect ones assisted by Si phonons are likely the dominant ones for freshly etched, H-passivated porous silicon where the Stokes shift is reported to be negligible or very small.^{10,26} For nanocrystals passivated with SiO₂, the Stokes shift is significant. A red shift of up to 1 eV for porous silicon oxidized in air has even been reported.²⁶ Thus, the dominant mechanism of emission must be different for H-passivated and SiO₂ passivated nanocrystals. However, we do not know the dependence of the oscillator strength with the diameter for SiO₂ passivated nanocrystals. We understand that the dominant emission here cannot be a quasidirect transition. Then, we will assume that somehow the “average” band gap determined from PLE is that of the nanocrystal with the average diameter. A comparison with the theoretically calculated band gaps will give a feeling of how crude this approximation is.

We obtain for the PLE band gap the following values: 1.95 ± 0.02 , 1.85 ± 0.02 , and 1.68 ± 0.04 eV for the 10%, 20%, and 30% supersaturation, respectively. We plot in Fig. 14 the theoretical results of the band gap versus nanocrystal diameter as obtained by different authors. The almost identical theoretical results obtained by Delerue *et al.*⁵⁴ and by

Wang and Zunger⁵⁵ by different calculation methods are probably the most accurate ones. We also plot the effective mass approximation of Takagahara and Takeda.⁵⁶ We also represent the PLE band gaps obtained by us (squares) and our experimental results coincide rather well with the theoretical predictions. We also plot in Fig. 14 the experimental PL peak position as a function of average diameter (circles). We observe an agreement in the tendency for both band gap and PL peak position versus diameter. First, this dependence with nanocrystal diameter corroborates that the transitions reported here are fundamental in a still indirect band-gap material. However, a remarkable fact is that the difference between band gap and PL emission, which is the Stokes shift, is approximately constant for all the samples and has a value of about 0.26 ± 0.03 eV.

Band to band indirect transitions are reported for porous Si from the resonantly excited PL experiments which clearly show the phonons of Si in the structure. For Si nanocrystals passivated with SiO₂ the indirect transitions could be assisted as well by the interaction of the electron–hole pairs with Si–O vibrations at the interface. This should be possible in a nanostructured material where volume and surface are strongly coupled.

Thus, the polar nature of the Si–O bond can make the trapping of the exciton favorable, via dipole–dipole attractive interaction, in the region adjacent to the interface Si–SiO₂. Somehow, the electron–hole pairs of the nanocrystals would couple the long-range field of the polar optical Si–O modes of the adjacent Si–SiO₂ interface in a way similar to electrons coupling phonons in polar or partly ionic crystals. We can think, as well, of the existence of vibronic interactions among electron–hole pairs created in the nanocrystals, and the polarizable matrix surrounding them. Thus, for an indirect transition in which phonon absorption is negligible one expects the threshold of the absorption coefficient to be situated at $E_g + E_p$, where E_g is the band gap and E_p is the energy of the phonon (or local vibration). Then, the emission of a photon with phonon emission should occur at the energy $E_g - E_p$, where the experimental Stokes shift would be $2E_p \approx 0.26$ eV and, consequently, $E_p \approx 0.13$ eV. This result coincides almost exactly with the energy of the Si–O vibration that is 0.134 eV. As $kT \approx 0.026$ eV, at room temperature, it is reasonable to assume that “phonon” absorption will be negligible. Kanemitsu has reported the emission spectra of SiO₂ capped nanocrystals resonantly excited and observed certain steps that can account for the interaction with SiO₂ vibrations.¹³ Finally, we want to stress that the existence of this recombination channel does not exclude the direct recombination or the recombination via a surface Si=O center, as pointed out in Ref. 26 for porous Si. We point out that direct zero phonon or quasidirect band to band recombination is small in Si nanocrystals due to the still indirect band gap. Furthermore, those kinds of Si=O centers are feasible in air oxidized porous silicon but much less probable in nanocrystals passivated with high quality thermal SiO₂.

VI. CONCLUSIONS

The experimental results reported in this article, their interpretation, and their correlation with theoretical models, configure a significant contribution to clarify the mechanism of the photoluminescence emission of ion beam synthesized silicon nanocrystals in SiO₂. We have reported reliable measurements of size distributions of Si nanocrystals embedded in SiO₂, which is of capital importance to quantify, interpret, and correlate many optical measurements. We have been able to measure the band gap and photoluminescence of Si nanocrystals in SiO₂ for different supersaturation and annealing times. We conclude that after 1 min of annealing at 1100 °C, the nucleation and pure growth stages of the nanocrystal population are almost over. For the rest of the annealing time, the nanocrystal ensemble evolves under a conservative asymptotic Ostwald ripening process. Nevertheless, the PL intensity increases for a significant amount of time and this has been correlated with the passivation of interfacial nonradiative defects, like the P_b centers measured by ESR. Annealing in forming gas is a short cut to obtain to the maximum possible PL yield with less thermal budget. The correlation between the average diameter of the nanocrystal population, the band gap, and the PL emission, strongly suggests that the dominant mechanism of emission for Si nanocrystals embedded in SiO₂ is a fundamental transition located at the interface with the assistance of a local Si–O vibration.

¹L. Brus in *Semiconductors and Semimetals*, edited by D. Lockwood (Academic, New York, 1998), Vol. 49, p. 303.

²S. Furukawa and T. Miyasato, *Phys. Rev. B* **38**, 5726 (1988).

³T. S. Iwayama, S. Nakao, and K. Saitoh, *Appl. Phys. Lett.* **65**, 1814 (1994).

⁴H. Takagi, H. Ogawa, Y. Yamazaki, A. Ishizadi, and T. Nakagiri, *Appl. Phys. Lett.* **56**, 2379 (1990).

⁵Z. H. Lu, *Nature (London)* **378**, 258 (1995).

⁶S. Hayashi, S. Tanimoto, M. Fujii, and K. Yamamoto, *Superlattices Microstruct.* **8**, 13 (1990).

⁷J. P. Proot, C. Delerue, and G. Allan, *Appl. Phys. Lett.* **61**, 1948 (1992).

⁸S. Iwayama, N. Kurumado, D. E. Hole, and D. E. Townsend, *J. Appl. Phys.* **83**, 6018 (1998).

⁹L. T. Canham, *Appl. Phys. Lett.* **57**, 1046 (1990).

¹⁰A. G. Cullis, L. T. Canham, and P. D. J. Calcott, *J. Appl. Phys.* **82**, 909 (1997).

¹¹Y. Kanemitsu, T. Ogawa, K. Shiraishi, and K. Takeda, *Phys. Rev. B* **48**, 4883 (1993).

¹²Y. Kanemitsu, *Phys. Rev. B* **53**, 13515 (1996).

¹³Y. Kanemitsu and S. Okamoto, *Phys. Rev. B* **56**, R1696 (1997).

¹⁴F. Koch and V. Petrova-Koch, *J. Non-Cryst. Solids* **198–200**, 840 (1996).

¹⁵A. Pérez-Rodríguez, B. Garrido, C. Bonafos, M. López, O. González-Varona, J. R. Morante, J. Montserrat, and R. Rodríguez, *J. Mater. Sci.* **10**, 385 (1999).

¹⁶B. Garrido, M. López, O. González, A. Pérez-Rodríguez, J. R. Morante, and C. Bonafos, *Appl. Phys. Lett.* **77**, 3143 (2000).

¹⁷M. López, B. Garrido, C. Bonafos, A. Pérez-Rodríguez, J. R. Morante, and A. Claverie, *Nucl. Instrum. Methods Phys. Res. B* **178**, 89 (2001).

¹⁸M. L. Brongersma, A. Polman, K. S. Min, E. Boer, T. Tambo, and H. A. Atwater, *Appl. Phys. Lett.* **72**, 2577 (1998).

¹⁹M. L. Brongersma, A. Polman, K. S. Min, and H. A. Atwater, *J. Appl. Phys.* **86**, 759 (1999).

²⁰S. Guha, M. D. Pace, D. N. Dunn, and I. L. Singer, *Appl. Phys. Lett.* **70**, 1207 (1997).

²¹S. Guha, *J. Appl. Phys.* **84**, 5210 (1998).

²²A. J. Kenyon, P. F. Trwoga, C. W. Pitt, and G. Rehm, *J. Appl. Phys.* **79**, 9291 (1996).

²³P. F. Trwoga, A. J. Kenyon, and C. W. Pitt, *J. Appl. Phys.* **83**, 3789 (1998).

- ²⁴S. Schuppler *et al.*, Phys. Rev. B **52**, 4910 (1995).
- ²⁵T. van Buuren, L. N. Dinh, L. L. Chase, W. J. Siekhaus, and L. J. Terminello, Phys. Rev. Lett. **80**, 3803 (1998).
- ²⁶M. V. Wolkin, J. Jorne, P. M. Fauchet, G. Allan, and C. Delerue, Phys. Rev. Lett. **82**, 197 (1999).
- ²⁷C. Bonafos, B. Garrido, M. López, A. Romano-Rodríguez, O. González, A. Pérez-Rodríguez, and J. R. Morante, Nucl. Instrum. Methods Phys. Res. B **147**, 373 (1999).
- ²⁸C. Bonafos, B. Garrido, M. Lopez, A. Perez-Rodriguez, J. R. Morante, Y. Kihn, G. Ben Assayag, and A. Claverie, Mater. Sci. Eng., B **69–70**, 379 (1999).
- ²⁹C. Bonafos, B. Garrido, M. López, A. Pérez-Rodríguez, J. R. Morante, Y. Kihn, G. Ben Assayag, and A. Claverie, Appl. Phys. Lett. **76**, 3962 (2000).
- ³⁰C. Bonafos *et al.*, Nucl. Instrum. Methods Phys. Res. B **178**, 17 (2001).
- ³¹G. Allan, C. Delerue, and M. Lannoo, Phys. Rev. Lett. **76**, 2961 (1996).
- ³²K. S. Min, K. V. Sheheglov, C. M. Yang, H. A. Atwater, M. L. Brongersma, and A. Polman, Appl. Phys. Lett. **69**, 2033 (1996).
- ³³S. P. Withrow, C. W. White, A. Meldrum, J. D. Budai, D. M. Hembree, Jr., and J. C. Barbour, J. Appl. Phys. **86**, 396 (1999).
- ³⁴S. Cheylan and R. G. Elliman, Appl. Phys. Lett. **78**, 1225 (2001).
- ³⁵B. Garrido, C. Domínguez, J. Montserrat, J. R. Morante, and J. Samitier, Phys. Rev. B **49**, 14845 (1994).
- ³⁶J. O. Malm and M. A. O'Keefe, Ultramicroscopy **68**, 13 (1997).
- ³⁷F. Iacona, G. Franzo, and C. Spinella, J. Appl. Phys. **87**, 1295 (2000).
- ³⁸L. A. Nesbit, Appl. Phys. Lett. **46**, 38 (1985).
- ³⁹M. Agarwal and S. T. Dunham, J. Appl. Phys. **78**, 5313 (1995).
- ⁴⁰N. E. B. Cowern, G. Mannino, P. A. Stolk, F. Roozeboom, H. G. A. Huizing, J. G. M. van Berkum, F. Cristiano, and A. Claverie, Phys. Rev. Lett. **82**, 4460 (1999).
- ⁴¹A. F. Leier, L. N. Safranov, and G. A. Kachurin, Semiconductors **33**, 380 (1999).
- ⁴²I. M. Lifshitz and V. V. Slyosov, J. Phys. Chem. Solids **19**, 35 (1961).
- ⁴³A. J. Ardell, Acta Metall. **20**, 61 (1972).
- ⁴⁴P. Bansal and A. J. Ardell, Metallography **5**, 97 (1972).
- ⁴⁵D. Kovalev, J. Diener, H. Heckler, G. Polisski, N. Künzner, and F. Koch, Phys. Rev. B **61**, 4485 (2000).
- ⁴⁶C. Delerue, G. Allan, and M. Lannoo, Phys. Rev. B **48**, 11024 (1993).
- ⁴⁷R. A. B. Devine, Jpn. J. Appl. Phys., Part 1 **31**, 4411 (1992), and references therein.
- ⁴⁸M. J. Uren, J. H. Stathis, and E. Cartier, J. Appl. Phys. **80**, 3915 (1996).
- ⁴⁹R. Czaputa, R. Fritzl, and A. Popitsch, Thin Solid Films **255**, 212 (1995).
- ⁵⁰S. M. Prokes, W. E. Carlos, and O. J. Glembocki, Phys. Rev. B **50**, 17093 (1994).
- ⁵¹W. E. Carlos and S. M. Prokes, J. Appl. Phys. **78**, 2129 (1995).
- ⁵²S. M. Prokes and W. E. Carlos, J. Appl. Phys. **78**, 2671 (1995).
- ⁵³A. Stesmans and V. V. Afanas'ev, Microelectron. Eng. **48**, 113 (1999).
- ⁵⁴C. Delerue, M. Lannoo, and G. Allan, Phys. Rev. B **48**, 11024 (1993).
- ⁵⁵L. W. Wang and A. Zunger, J. Phys. Chem. **98**, 2158 (1994).
- ⁵⁶T. Takagahara and K. Takeda, Phys. Rev. B **46**, 15578 (1992).